ELSEVIER

Journal of Nuclear Materials 256 (1998) 180–188

journal of nuclear materials

Microstructure and nanohardness of hafnium diboride after ion irradiations

P. Cheminant-Coatanlem [a,*], L. Boulanger [b], X. Deschanels [a], A. Thorel [c]

[a] *Commissariat à l'énergie atomique, DRN/DMT/SEMI/LEMA, F-91191 Gif sur Yvette cedex, France*
[b] *Commissariat à l'énergie atomique, DTA/CEREM/DECM/SRMP, 91191 Gif sur Yvette, France*
[c] *Centre des matériaux Pierre-Marie Fourt, Ecole des Mines de Paris, BP 87, 91003 Evry cedex, France*

Received 14 January 1998; accepted 3 April 1998

Abstract

In order to simulate helium and lithium appearance originating from the ^{10}B (n,α)^{7}Li reaction, that occurs under neutron irradiation in a PWR, hafnium diboride samples have been irradiated with He^+ and Li^+ ions at 350°C. As implanted and annealed materials have been characterised by TEM observations and nanohardness measurements. In spite of high concentration of implanted helium, no helium bubbles were found whereas the TEM images showed a contrast associated with tiny dislocation loops. Observation on samples annealed at 1600°C allowed a more detailed analysis of loops which exhibit an interstitial nature (resp. vacancy) for a $\{1\ 1\ \bar{2}\ 0\}$ or $\{1\ 0\ \bar{1}\ 0\}$ habit plane (resp. (0 0 0 1)). The organisation of these secondary defects leads to a strongly anisotropic deformation of grains which is thought to cause intergranular microcracking when conflictual stresses are met at grain boundaries.

1. Introduction

This study concerns materials for control-rod applications in 100% MOX pressurised water reactors (PWR). Hafnium diboride appears to be a promising candidate since it exhibits a high melting point ($T_m = 3380$°C) [1] and a high neutron absorber efficiency, equivalent to that of boron carbide commonly used in the present PWR [2]. Furthermore the new absorber must be able to withhold the corrosion mechanisms of the PWR core environment, i.e. water, with LiOH and H_3BO_3 in solution, at 350°C and under 155 bars. It has been observed that metal-rich pellets of HfB_2 + 10 vol% Hf fulfilled these requirements [3]. All these observations let us think that HfB_2 based materials could be appropriate neutron absorbers.

Investigations on neutron irradiated boron carbide and borides of transition metals have been carried out at the Vallecitos Atomic Laboratory of the General Electric Company in the 1960s [4]. The first post-irradiation analysis showed that diborides had swelled less and released few helium compared to B_4C. By X-ray diffraction, the authors also demonstrated that the crystalline structure in diborides had collapsed less than that of hexa- and dodecaborides. The better behaviour (helium release, lattice resistance,...) of diborides compared to the others under irradiation is explained by the fact that diborides crystallise in a compact structure with a high bonding strength.

Following these former investigations it seems reasonable to assume that, as it is observed in B_4C, HfB_2 swelling is the direct consequence of the He and Li appearance and the subsequent bubble formation, resulting from $^{10}B(n,\alpha)^{7}Li$ reaction. To ascertain this assumption and to determine the specific role of each (n,α) reaction product in the HfB_2 structural damaging, He^+ and Li^+ have been implanted separately on thin TEM samples for further microstructural observations. In addition, nanohardness tests have been carried out on the thin He implanted layer of the HfB_2 samples.

* Corresponding author. Tel.: +33-1 69 41 21 77; e-mail: pascale.coatanlem@wanadoo.fr.

0022-3115/98/$19.00
PII: S0022-3115(98)00059-2

Table 1
Sintering and chemical analysis of pellets

Powders		HfB_2	HfB_2 + 10 vol.% Hf
Sintering	T (°C)	2000	1800
	t (min)	60	15
	P (bars)	670	470
Annealing	T (°C)	–	1200 (24 h)
Chemical Analysis (wt%)	Metallic impurities	0.53	0.84
	C	0.20	0.28
	O	0.28	0.34
	B/Hf	1.98	1.85
d/d_0 [a] (%)		95	98
Pellets		S-HfB_2	MR-HfB_2

[a] $d_0 = 11.2$ g/cm^3.

2. Materials

Powders were supplied by CERAC Company. In order to obtain high density pellets (>95% of the theoretical density), HfB_2 powder and a mixture of HfB_2 + 10 vol.% Hf were hot-pressed at respectively, 2000°C and 1800°C. The MR-HfB_2 (metal-rich samples: HfB_2 + 10 vol.% Hf) were then annealed 24 h at 1200°C to homogenise the microstructure. Sintering and heat treatment conditions are given in Table 1. Chemical analysis of O and C by infra-red absorption spectrometry and of metallic impurities by ICP-atomic emission spectrometry are also mentioned.

X-ray spectra, displayed in Fig. 1, reveal that the S-HfB_2 pellets (stoichiometric HfB_2) are single-phased, while several phases appear in the MR-HfB_2: hexagonal HfB_2, hexagonal Hf, monoclinic HfO_2 and a face-centered cubic phase. The latter corresponds to the FCC HfB phase stabilised by impurities such as O, C or N, as described by Glaser [5]. Optical micrographs of the MR-HfB_2 clearly reveal these secondary phases whose composition, obtained through electron microprobe analysis, is consistent with Hf, HfB and HfO_2 embedded in the HfB_2 matrix. The general microstructure of S-HfB_2, revealed by optical microscopy after etching (1 HNO_3, 1 HF and 3 lactic acid) (Fig. 2), consists of an array of 10 μm wide equiaxed grains. In contrast, the grain size of the MR-HfB_2 samples ranges from 0.1 to 30 μm with heterogeneous grain distribution of shape and size.

3. Experimental procedure

3.1. Sample preparation

Diamond impregnated tools were used to cut 250 μm thick slices from the pellets. Samples of 3 mm in diameter are then obtained by ultrasonic grinding.

TEM specimens were electropolished in a TENUPOL apparatus at −30°C under 70 V, in a solution made of 70 vol.% ethanol, 20 vol.% butoxyethanol and 10 vol.% perchloric acid. Conventional TEM observations are carried out at 200 keV in a CM 20 Philips electron microscope. Only the HfB_2 matrix is observable in the MR-HfB_2 samples since only this phase dissolves by electrochemical etching.

The nanohardness experiments have been performed only on S-HfB_2 samples. The surface of which was diamond polished (15–1/4 μm).

3.2. Irradiations

The samples are irradiated with 550 keV He^+ ions in a van de Graaff accelerator. In order to disperse and decrease the incident He^+ ion energy (55 keV), a degrader made of a 1.6 μm thick Al foils is placed between the He beam and the samples. The helium distribution has been estimated by the TRIM 91 software [6]: calculations give an extention of 200 nm with a peak of concentration at 100 nm. Mean concentrations in the samples are given in Table 2.

Identical experiments have been carried out with 40 keV Li^+ ions, without using a degrader, in an accelerator. The concentration of implanted lithium has been

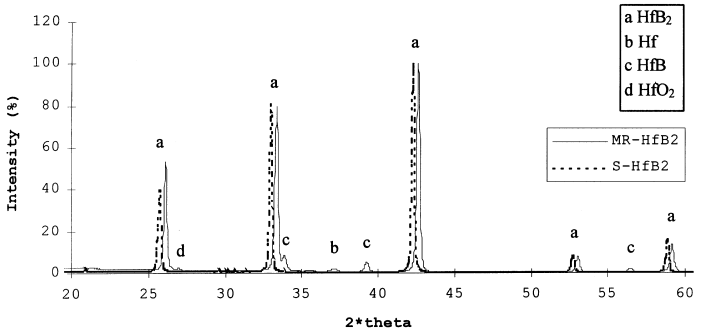

Fig. 1. (a) X-ray diffraction performed on S-HfB_2 pellets, (b) on MR-HfB_2 pellets.

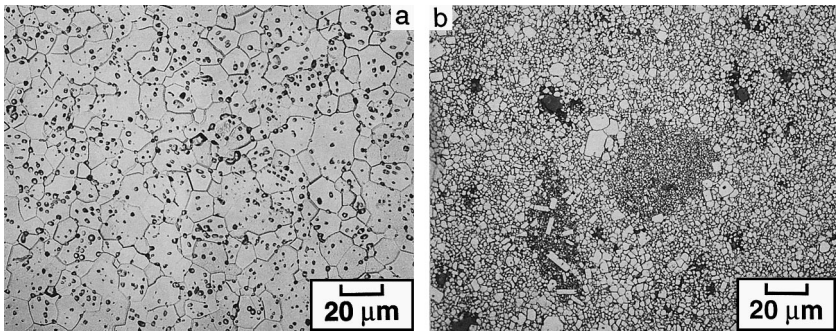

Fig. 2. (a) Optical micrograph of S-HfB_2 samples, (b) optical micrograph of MR-HfB_2 samples.

Table 2
Ion irradiation conditions

Material	T_{irr} (°C)	Ion concentration (at.%)	Fluence (ion/cm^2)	Use
S-HfB_2	30 [a]	0.5	10^{16}	
	350			
MR-HfB_2	30 [a]	0.5	10^{16}	TEM
	350			study
S-HfB_2	350	10	2×10^{17}	
MR-HfB_2	350	10	2×10^{17}	
		1	2×10^{16}	
S-HfB_2 [a]	350	2	4×10^{16}	Nanohardness
		5	10^{17}	
		10	2×10^{17}	

[a] He^+ irradiation only.

chosen to be equivalent to that of implanted helium. Both lithium and helium profiles appear to be almost identical.

Except for low fluence He implantations carried out at 30°C, all the irradiations have been performed at 350°C to simulate the environmental temperature of a PWR core.

3.3. Annealing

Annealing of TEM thin foils up to 1000°C is performed in the TEM Gatan heating stage while an induction furnace is used for annealing above 1200°C. A high vacuum (10^{-7} Torr) is maintained in the furnace by a turbo-molecular pump.

3.4. Nanohardness

Nanohardness measurements are achieved by means of the Nanotest 550 from Micro Materials Ltd., according to the principle developed by Pollock [7]. This tester is equipped with a Berkovitch diamond indenter. Tests are calibrated to investigate the material at a depth of 100 nm that corresponds to the maximum of the implanted helium profile. Nanohardness values are drawn from the charge–displacement graphs and are calculated using a software based on the equations of Pharr and Oliver [8]. The final nanohardness is a value averaged over 40 measurements per irradiation fluence. The results are compared to those obtained from the non-irradiated samples.

4. Results

4.1. TEM observations of He^+ irradiated foils

4.1.1. As received states

Observations of S-HfB_2 specimens before irradiation show featureless grains and triple junction (Fig. 3(a)). The HfB_2 grains in MR-HfB_2 display 15 nm intragranular voids heterogeneously distributed as well as large cavities associated with precipitates identified by PEELS and microdiffraction as HfO_2 (Fig. 3(b)).

4.1.2. Irradiated states

4.1.2.1. Low fluence. The He^+-particle injection causes the appearance of numerous black dots (Fig. 4(a)) in the grains of S-HfB_2. The apparent density of this secondary defect structure depending on the orientation of the electron beam, it is concluded that they are crystallography related. No helium bubble is observed.

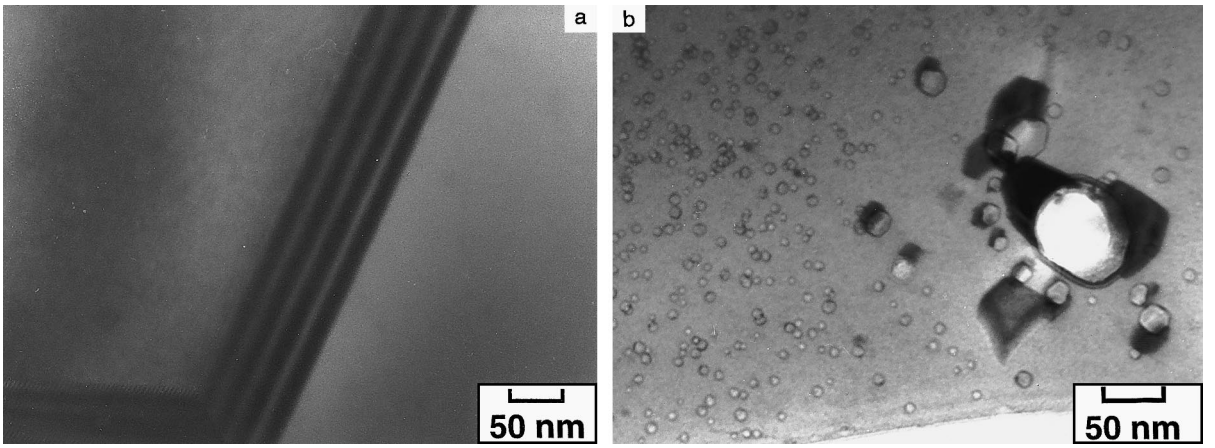

Fig. 3. (a) TEM micrographs of S-HfB_2 samples, (b) TEM micrographs of HfB_2 grains in MR-HfB_2 samples.

Voids in the grains of MR-HfB_2 appear non-affected by the irradiation.

4.1.2.2. High fluence. No helium bubbles are found in the grains of S-HfB_2, in spite of the high concentration of implanted helium. Nevertheless, small dots display a contrast of dislocation loops (Fig. 4(b)). As a result of the He^+ implantation in an area localised 200 nm below the surface, the specimens appear strongly bent in the direction of the ion beam.

4.1.3. Annealing of irradiated states

4.1.3.1. Low fluence observations. All the samples irradiated at low fluence have been annealed 1 h at 1600°C (0.51 T_m). Helium bubbles appear at grain boundaries and small dots have transformed into resolved dislocation loops. When these loops are edge-on, an associated strain field is observed, as shown in Fig. 5(b). It is noticed that loops in MR-HfB_2 are much smaller than those in S-HfB_2 (Fig. 6). Therefore the dislocation loops analysis (Burgers vector and nature of loops) has been carried out on the stoichiometric samples, as illustrated in Fig. 5.

Dislocation loops analysis: Two populations of perfect loops are found. The first population (Fig. 5(b)) is invisible with $\vec{g} = \langle 1\,0\,\bar{1}\,0\rangle$ and $\vec{g} = \langle 1\,1\,\bar{2}\,0\rangle$. These loops are *c* type loops with Burgers vector $\vec{b} = [0\,0\,0\,1]$. Tilting the samples allows us to identify their habit plane which is found to be $(0\,0\,0\,1)$. It is thus concluded that they are pure edge dislocation loops. The second population of loops (Fig. 5(a)) is distributed on three habit planes. The first part of these loops is extinguished for $\vec{g} = [1\,0\,\bar{1}\,0]$, the second is invisible for $\vec{g} = [1\,\bar{1}\,0\,0]$ and the third for $\vec{g} = [0\,1\,\bar{1}\,0]$. All of them are invisible for $\vec{g} = [0\,0\,0\,1]$. Their Burgers vector is thus determined as $\vec{b} = \lambda[1\,1\,\bar{2}\,0]$. These loops are *a* type loops and have their normals distributed between the $\langle 1\,0\,\bar{1}\,0\rangle$ and $\langle 1\,1\,\bar{2}\,0\rangle$directions. They are therefore of mixed character.

The inside–outside contrast method, introduced by Groves and Kelly [9], is used to determine the nature of the dislocation loops. This method is based on the

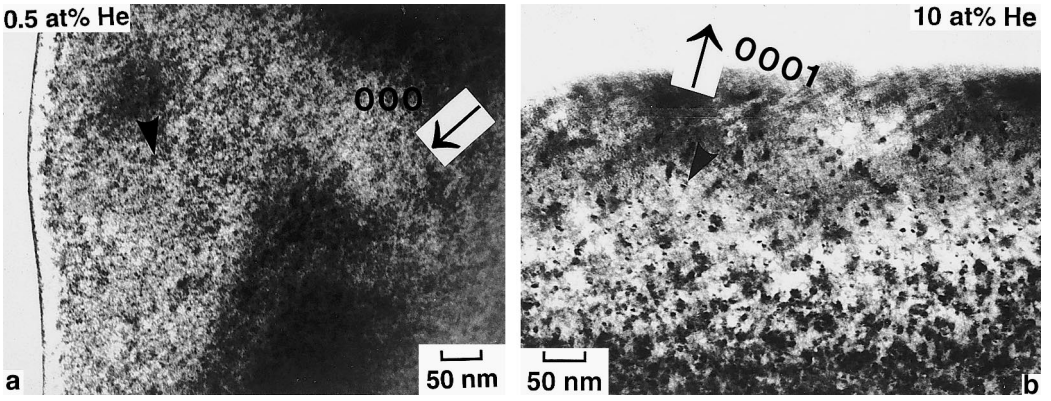

Fig. 4. As irradiated S-HfB_2 foils: (a) at low fluence, small dots appear: (b) at high fluence, tiny dislocation loops are observed.

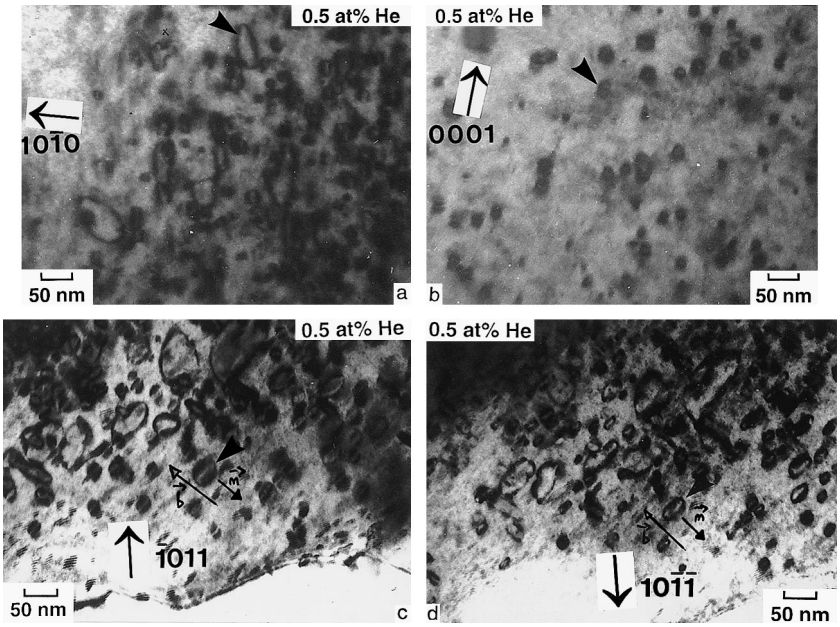

Fig. 5. Foils of S-HfB_2 irradiated at low fluence and annealed at 1600°C: (a) *a* type loops; (b) *c* type loops; (c) and (d) determination of loop nature by inside–outside method contrast.

fact that, under diffraction conditions, the image contrast of a dislocation loop lies either inside or outside the true loop position as projected onto the image plane, depending on (i) the type of the loop, (ii) its orientation with respect to the electron beam and the operating diffraction vector, $\vec{g}$ and (iii) the sign of the excitation error *s*. As shown in Fig. 5(c), *a* type and *c* type loops were observed with $\vec{g} = \langle 1\,0\,\bar{1}\,1\rangle$. FS-RH rule ('first hand-right hand' rule) is applied in order to define the Burgers vector of the loops. The loop nature is then determined by applying $(gb)s$ rule [10]. The *c* type loops appear to be vacancy loops.

The determination of the nature of the *a* type loops of the second population is more difficult because of their mixed character and of their localisation in rather thick areas. Those loops seem to be mostly interstitial and few of them appear to be vacancy loops.

Loop concentration is given in Table 3 and determined on annealed samples, because black dots in as-implanted samples are too numerous and too tiny to be numbered. Their concentration is measured on micrographs when loops are nearly edge-on and excited by $\vec{g} = \langle 1\,0\,\bar{1}\,0\rangle$ for *a* type dislocations and $\vec{g} = [0\,0\,0\,1]$ for *c* type dislocations. Loop sizes after annealing at 1600°C are given in Table 4. All these results make possible a comparison between the stoichiometric and metal-rich specimens: it is noticed that the loop diameters in stoichiometric samples range from 6 to 50 nm whereas they are limited to 2 nm in metal-rich specimens. This

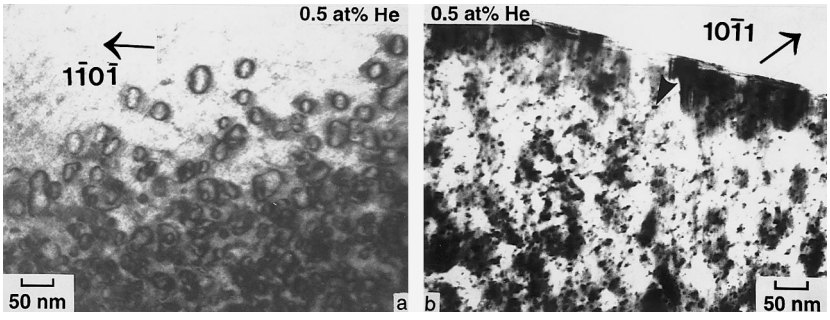

Fig. 6. Comparison of loop sizes in S-HfB_2 foils (a) and in HfB_2 grains of MR-HfB_2 sample (b), irradiated at low fluence and annealed at 1600°C.

Table 3
Loop concentrations and dislocation line densities in He^+ irradiated samples, annealed at 1600°C

Material	He concentration (at.%)	*c* type loop concentration (cm^{-3})	*a* type loop concentration dislocation (cm^{-3})	*a* type line density cm^{-2})
S-HfB_2	0.5	6×10^{15}	5×10^{15}	
MR-HfB_2	0.5	2×10^{16}	10^{16}	
S-HfB_2	10	6×10^{15}		4×10^{10}
MR-HfB_2	10	0		4×10^{9}

Table 4
Mean size of dislocation loops in He^+ irradiated samples, annealed at 1600°C

Material	He concentration (at.%)	*c* type loop (nm)	*a* type loop (nm)
S-HfB_2	0.5	17	37
MR-HfB_2	0.5	<5	<2
S-HfB_2	10	5,8	–
MR-HfB_2	10	0	–

size difference between loops from both materials is clearly evidenced in Fig. 6.

The comparison between *a* type and *c* type loops shows that their concentrations are equivalent. But *c* type loops seem to be smaller than *a* type loops in the S-HfB_2 foils. In the MR-HfB_2 foils, loops are too small to enable size comparison.

The deformation ε along the *c*-axis direction due to the vacancy loops can be calculated on the basis of the following relation:

$$\varepsilon = -\frac{1}{3}\frac{c_b}{n}\left(\frac{d}{a}\right)^2,$$

where c_b is the loop concentration per unit volume, *n* the number of atoms per unit volume (10^{23} cm^{-3}), *d* the mean loop diameter and *a* the lattice parameter (0.314 nm). It is then inferred that the vacancy loops induce a *c*-axis contraction of 5.9×10^{-5} for a mean loop diameter equal to 17 nm.

4.1.3.2. High fluence observations:. Annealing from 350°C to 1800°C has been performed in order to grow bubbles until they can be observed. Image from bubbles is obtained with no Bragg reflection and observing the phase contrast of Fresnel fringes which appears during underfocussing. At 1200°C, bubbles appear uniformly distributed in grains and at grain boundaries. Above 1500°C, two populations of bubbles develop: small 2 nm wide bubbles (even smaller in the bulk) and large faceted bubbles (Fig. 7(c)). Grain boundaries and dislocations seem to be preferential sites for bubble growth. It has been observed that MR-HfB_2 foils display smaller bubbles than S-HfB_2 samples and that cavities can easily be distinguished from bubbles because of a significant size difference. Secondary defect structure has also changed after annealing and, at 1600°C, *c* type loops have a strong tendency to disappear, while *a* type loops have condensed into a tight network (Fig. 7(a)(b)).

Dislocation loop analysis: In S-HfB_2 foils, *c* type loops after annealing at 1600°C display a mean size of 5.8 nm (Table 4) and a concentration of 6×10^{15} cm^{-3} (Table 3). In MR-HfB_2 samples, *c* type loops have disappeared after annealing. The density of *a* type dislocation network is also given in Table 3 and it appears smaller in HfB_2 grains of MR-HfB_2 foils than in S-HfB_2 samples. A comparison between samples irradiated at different fluences shows that the concentration of *c* type loops in S-HfB_2 foils is unchanged as a function of the irradiation fluence, but loops sizes decrease with increasing irradiation fluence. In MR-HfB_2 samples, *c* type loop concentration decreases down to 0 with increasing irradiation fluence.

Helium bubble analysis: The two populations of bubbles have been analysed on S-HfB_2 foils. All the large bubbles are faceted: their projection on the basal plane is hexagonal and rectangular on prismatic planes. After annealing from 1200°C to 1800°C, bubble concentration has been estimated from TEM micrographs: Fig. 8 displays the plots of small and large bubble concentration as a function of the annealing temperature.

4.2. TEM observations on Li^+ irradiated foils

4.2.1. As irradiated states

No precipitates have been found after Li^+ irradiations at 350°C, even in high fluence irradiated samples. Nevertheless, the same secondary defect structure as in He^+ irradiated foils is observed. The lithium implanted foils display the very same bending as with He^+ ions.

4.2.2. In situ annealing:

TEM observations, during in situ annealing from 350°C to 1000°C, have shown that no precipitation of

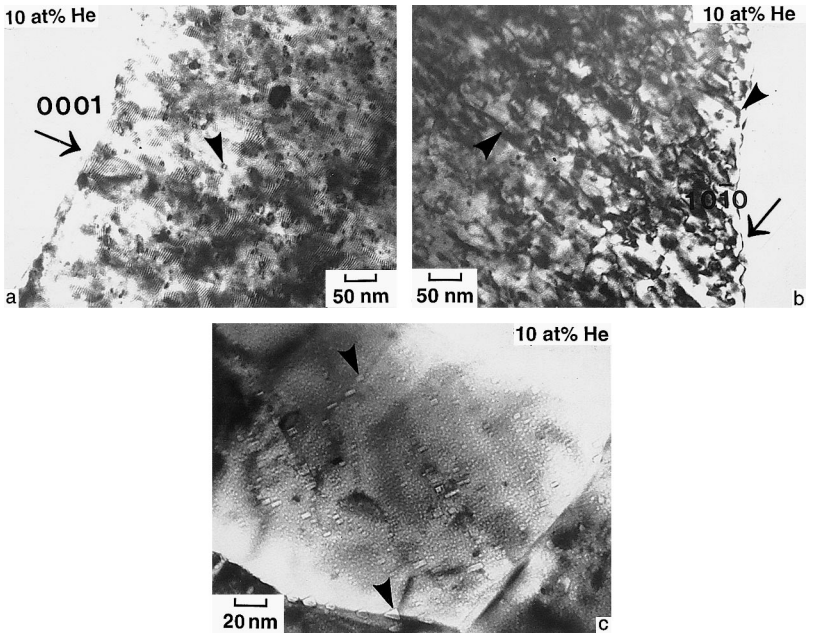

Fig. 7. Foils of S-HfB_2 irradiated at high fluence and annealed at 1600°C: (a) *c* type loops; (b) *a* type dislocation network; (c) two populations of helium bubbles.

lithium occurs, neither in the foils implanted at high fluence. Yet it seemed that small dot concentration decreases after annealing as observed in helium irradiated foils.

4.3. Nanohardness results

The histograms of the nanohardness results are given in Fig. 9. Except for the sample implanted at 1 at.% of He, measurements are not very dispersed. We observe that the mean value of nanohardness of non-irradiated HfB_2 is equal to 32.5 GPa. Mean nanohardness values are higher in implanted samples, it increases with implanted helium concentration as seen in Fig. 10. This increase saturates at 45 GPa above about 5 at.% implanted helium.

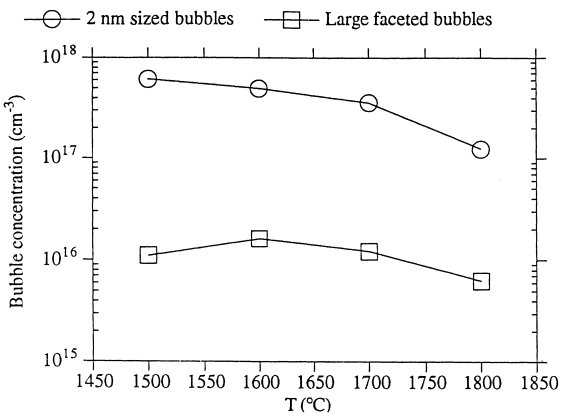

Fig. 8. Bubble concentrations versus annealing temperature in high concentration implanted foils of S-HfB_2.

5. Discussion and conclusion

In the early stage of this study, He bubbles were supposed to be responsible for the swelling of HfB_2 observed on samples after neutron irradiation [4]. In fact, we referred to the observations on B_4C, where He forms pressurised bubbles after He^+ irradiation at 750°C [11]. However, no bubbles have been found before annealing, even in foils implanted up to 10 at.%. He bubbles only appear after annealing performed at a high temperature (from 1200°C) in comparison with the temperature of PWR core (350°C). Vacancy diffusion before 1200°C may be too slow to allow significant growth of He bubbles. In addition, no pressurised bubbles have been found. Thus it seems that He bubble growth has to be largely assisted by vacancy supply. This observation is also supported by the fact that, in high concentration implanted samples, vacancy loops tend to disappear and interstitial loops transform into a dense dislocation network after annealing. Loops are thus vacancy sources for He bubble growth. This explains the trend of He bubbles to grow on dislocations and at grain boundaries where vacancies are easily delivered. In metal-rich samples, voids are observed in HfB_2 grains before irradiation. Bubbles, observed in post-irradiation annealed

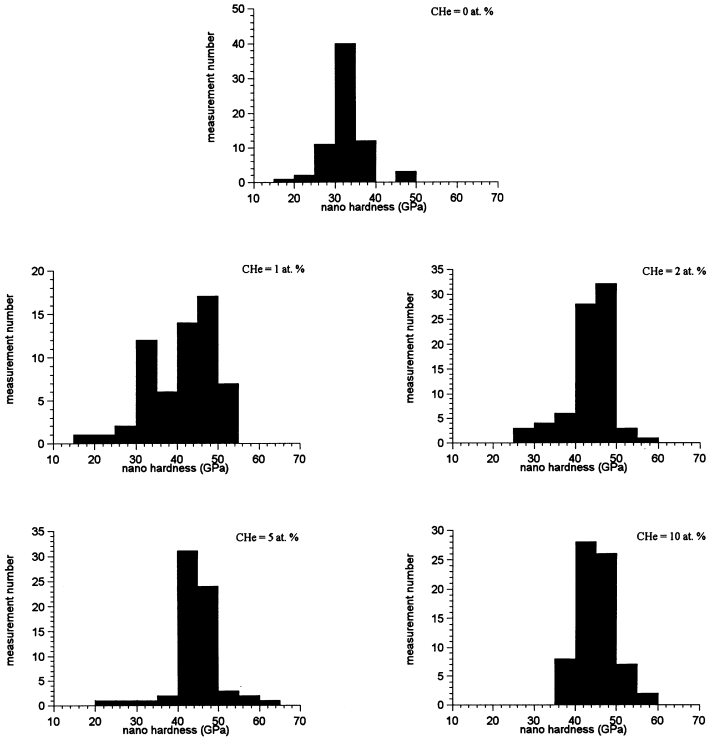

Fig. 9. Histograms of nanohardness data from measurements 70 on helium implanted samples.

samples, are smaller in MR-HfB_2 foils than in S-HfB_2 specimens. Voids are likely to be sinks for implanted He atoms.

Implantations of lithium also give as a result that no precipitation at irradiation temperature occurs in HfB_2 grains. Similarly, annealing does not authorise the precipitation of lithium. It has already been observed that such an element with no chemical affinity with refractory material diffuses out of the pellets without forming precipitates [4,12].

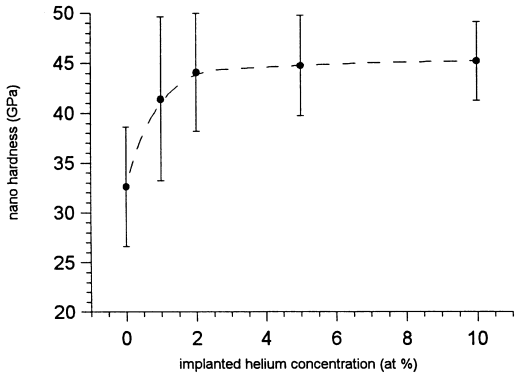

Fig. 10. Nanohardness data versus implanted helium concentration.

The fact that neither helium bubbles nor lithium precipitates were found in as-implanted foils makes us think that the contribution of loops to radiation-induced damage in HfB_2 must be important at the operating temperature of a PWR. On TEM micrographs, after irradiations at 30°C and 350°C, they look like small dots that are unresolved dislocation loops. The analysis of these loops is thus performed on annealed samples and therefore may be disturbed by He bubble growth that requires vacancies: *a* type dislocation network and disappearance of *c* type vacancy loops in high fluence irradiated samples are artefacts of annealing. Thus, the primary radiation-induced defect structure forms dislocation loops. The loops of both natures, interstitial and vacancy, have a specific organisation in the hexagonal lattice of HfB_2. Vacancy loops lay on basal planes while habit planes of interstitial loops are perpendicular to basal planes. Thus an anisotropic deformation of the grains occurs under irradiation: contraction of the grains in *c*-direction and dilatation in *a*-directions. This phenomenon has been observed in hexagonal metals such as Zr [13] and Ti [14]. In Zircaloy used for nuclear applications, the macroscopic consequence is the growth of textured clads. In agreement with us, American authors [4] also observed by X-ray analysis a contraction in the *c*-direction and a dilatation in the *a*-direction of the lattice. Such a grain deformation develops stress in grains.

Thus, the swelling of HfB_2 pellets after neutron irradiation observed by the American team [4] cannot be explained by the formation of helium bubbles at the irradiation temperature of 350°C. In fact, helium is a voluminous atom (0.93 Å) compared to the interstitial sites in HfB_2 lattice (0.7 Å). Helium implantation induces the dilatation of HfB_2 lattice that is pointed out by the foil bending.

In HfB_2 grains of the MR-HfB_2 samples, the secondary radiation-induced defects form smaller dislocation loops than those observed in S-HfB_2 foils. Cavities seem to be sinks for point defects as well as for implanted atoms. Such an interaction between point defects and cavities suggests that HfB_2 grain deformation in MR-HfB_2 samples will be less important and then fracturation at grain boundaries will occur for bigger irradiation fluences than in S-HfB_2 specimens.

Nanohardness data show the hardening of HfB_2. This must be related to the post-irradiation TEM observations: irradiation induces the formation of dislocation loops associated with a strain field which increases locally the hardness of the grains.

Acknowledgements

To Yves Serruys (DTA/CEREM/DECM/SRMP – CEA-Saclay) for the He^+ irradiations, to Sylvie Poissonnet (DTA/CEREM/DECM/SRMP – CEA-Saclay) for nanohardness measurements and to Odile Kaïtasov (CSNSM-CNRS – Paris XI) for the Li^+ irradiations.

References

[1] E. Rudy, T. Windisch, Technical Report No. AFLM-TR-65-2, Part II, Vol. XIII, 1966.
[2] D. Azzoug, J. Porta, private communication, 1992.
[3] X. Deschanels, Key Engineering Materials, vol. 113, TransTech Aedermannsdorf, 1996, p. 189.
[4] E.W. Hoyt, D.L. Zimmerman, Radiation Effects in Borides, Vallecitos Atomic Lab. Report GEAP-3749, Part I, 1962.
[5] F.W. Glaser et al., J. Met. (1953) 1119.
[6] J.F. Ziegler, J.P. Biersack, U. Littmark, The Stopping and Range of Ions in Matter, Pergamon Press, New York, 1985.
[7] D. Newey, M.A. Wilkins, H.M. Pollock, J. Phys. E: Sci. Instr. 15 (1982) 119.
[8] G.M. Pharr, W.C. Oliver, MRS Bull. (1982) p. 28.
[9] G.W. Groves, A. Kelly, Philos. Mag. 6 (1961) 1527.
[10] H. Foll, M. Wilkens, Phys. Stat. Sol. (a) 31 (1975) 519.
[11] T. Stoto, CEA Report No. 5382, 1987.
[12] T. Stoto, N. Housseau et, L. Zuppiroli, J. Appl. Phys. 68 (7) (1990) 3198.
[13] A. Jostson, P.M. Kelly, R.G. Blake, J. Nucl. Mater. 66 (1977) 236.
[14] M. Griffiths, D. Faulkner, R.C. Styles, J. Nucl. Mater. 119 (1983) 189.